

# Unconventional band structure and pseudogap of liquid metals on a crystalline insulator

Keun Su Kim (✉ [keunsukim@yonsei.ac.kr](mailto:keunsukim@yonsei.ac.kr))

Yonsei University <https://orcid.org/0000-0002-7033-1177>

Sae Hee Ryu

Pohang University of Science and Technology <https://orcid.org/0000-0003-3207-7582>

Minjae Huh

Pohang University of Science and Technology <https://orcid.org/0000-0002-0362-9205>

Do Yun Park

Yonsei University

Chris Jozwiak

Advanced Light Source, Lawrence Berkeley National Laboratory <https://orcid.org/0000-0002-0980-3753>

Eli Rotenberg

E. O. Lawrence Berkeley National Laboratory <https://orcid.org/0000-0002-3979-8844>

Aaron Bostwick

Lawrence Berkeley National Laboratory <https://orcid.org/0000-0002-9008-2980>

---

## Research Article

**Keywords:** band structure, liquid metals, crystalline insulator

**Posted Date:** September 11th, 2020

**DOI:** <https://doi.org/10.21203/rs.3.rs-75224/v1>

**License:**  This work is licensed under a Creative Commons Attribution 4.0 International License.

[Read Full License](#)

---

**Version of Record:** A version of this preprint was published at Nature on August 4th, 2021. See the published version at <https://doi.org/10.1038/s41586-021-03683-0>.

# Abstract

A key to understand how electrons behave in crystalline solids is the band structure that connects the energy of electron waves to their wavenumber ( $k$ ). Even in the phase of matter with only short-range order (liquid), the coherent part of electron waves still possesses a band structure. Theoretical models for the band structure of liquid metals were formulated more than 5 decades ago<sup>1-15</sup>, but so far, it has remained unobserved experimentally. Here, we reveal the band structure of liquid metals using the interface between liquid dopants (alkali metals) and a crystalline insulator (black phosphorus). We find that the conventional parabolic band structure of free electrons bends back towards zero  $k$  with the isotropic pseudogap of 30-240 meV from the Fermi level. This is the  $k$  renormalization caused by resonance scattering that leads to the formation of quasi-bound states in the scattering potential of liquid alkali-metal ions. The depth of this potential tuned by different kinds of alkali metal (Na, K, Rb, and Cs) allows us to classify the pseudogap of  $p$ -wave and  $d$ -wave resonance. Our results provide a key clue to the pseudogap phase of various materials<sup>16-20</sup>, a common aspect of which is the crystalline insulator doped by disordered (liquid) dopants.

## Main Text

In 1960s, there was a series of pioneering theoretical works for the band structure of liquid metals<sup>1-9</sup>. Like glassy materials have a well-defined complex refractive index, electron waves under the influence of multiple scattering acquire a complex wavenumber shift  $Dk$  whose magnitude is sizable at resonance. As shown in Fig. 1a, the band structure of free electrons ( $E \sim k^2$ ) is distorted by the real part of  $Dk$  [ $\text{Re}(Dk)$ ] in an unusual sinusoidal form that has no counterpart in crystalline solids. The corresponding imaginary part of  $Dk$  [ $\text{Im}(Dk)$ ] represents a spread of  $k$  related to the formation of quasi-bound states (QBS) around liquid ions. In the density of states (inset in Fig. 1a), a local minimum is formed at a resonance energy ( $E_r$ )<sup>5,9-12</sup>, which is the “pseudogap” coined by Mott<sup>13,14</sup>. This backward-bending band dispersion with pseudogap should be observable by means of angle-resolved photoemission spectroscopy (ARPES). Although ARPES was used to study the melting transition of a metal monolayer<sup>21,22</sup>, the characteristic band structure depicted in Fig. 1a has not been observed.

A key idea in our experiments is to study the interface between liquid dopants (alkali metals) and a crystalline insulator (black phosphorus)<sup>23-26</sup>. Black phosphorus is a stack of van-der-Waals layers, in which the honeycomb lattice of P atoms is regularly modulated to form a one-dimensional array of atomic-scale zigzag ridges and valleys (Fig. 1b). The alkali-metal atoms are adsorbed in the valley along which they are nearly free to move with the diffusion barrier as low as 25 meV<sup>26</sup>. The distribution of alkali-metal atoms on black phosphorus is known to show the oval-shape structure factor (Fig. 1c) at low temperature (above 10 K)<sup>25</sup>. This is the defining characteristic of liquid (disordered) phases with short-range order<sup>27,28</sup>, which is clearly distinct from both crystalline and fully random cases (Extended Data

Fig. 1). Given the situation (Fig. 1b), the metallic (doped) electrons in black phosphorus are subject to multiple scattering by the potential of liquid dopants, which is the focus of our study.

In the simple picture of surface doping that has been widely accepted so far, the conduction bands in the surface layer of black phosphorus adjacent to alkali-metal dopants shift below the Fermi energy  $E_F$ . Figure 1d shows constant-energy contours at  $E_F$  (the Fermi surface)<sup>23,24</sup> expected for surface-doped black phosphorus at the electron density  $n_e$  of  $1.0 \times 10^{14} \text{ cm}^{-2}$ . There is a large oval-shape contour centred at the G point (labelled C1) with a pair of small pockets separated along the  $y$  axis (labelled C2). The energy dispersion of C1 and C2 bands is shown in Fig. 2a-c along 3 high-symmetry directions ( $k_y$ ,  $k_s$ , and  $k_x$  as indicated in Fig. 1d), respectively. Owing to the crystal symmetry of black phosphorus, the band dispersion of C1 changes from quadratic in  $k_y$  (Fig. 2a) to linear in  $k_x$  (Fig. 2c)<sup>23</sup>. A set of  $k$  at  $E_F$  (or  $k_F$ ) in every in-plane direction constitutes the oval-shape Fermi contour of C1 in Fig. 1d.

Figure 2d-o displays a series of ARPES data taken from bulk black phosphorus whose surface is doped by different kinds of alkali metal (Na, K, Rb, and Cs), as marked at the bottom right of each panel. In data for Na taken along  $k_y$  (Fig. 2d), there is a clear signature of C2 bands at  $\pm 0.6 \text{ \AA}^{-1}$ , as expected in Fig. 2a. In contrast, a striking deviation from the expected in Fig. 2a is observed for the C1 band. Unlike the sharp Fermi-Dirac cut-off of C2 bands that can be used as an internal reference of  $E_F$ , the C1 band shows a gaplike feature with the magnitude of at least 0.2 eV from  $E_F$ . More noteworthy is that the band dispersion of C1 bends back at around -0.2 eV towards  $k = 0$  or the G point with a weak intensity. This backward-bending dispersion of the C1 band can be seen more clearly in  $k_s$  (Fig. 2e) with a diminishing intensity towards  $E_F$ , and intriguingly even reaches close to  $k = 0$  in  $k_x$  (Fig. 2f).

On the other hand, a difference from the Na case is observed for black phosphorus doped by K, Rb, and Cs. In data taken along  $k_y$  (Fig. 2g,j,m), there is commonly a pair of C2 bands crossing  $E_F$ , as observed in Fig. 2d. However, the C1 band shows a well-defined energy gap with no sign of the backward-bending band dispersion, as the ARPES intensity diminishes more abruptly towards  $E_F$ . The magnitude of energy gaps is about 65-70 meV for K and Rb, and about 30 meV for Cs, which are clearly smaller than 200 meV in the Na case (Fig. 2d). A series of ARPES data taken along  $k_s$  (Fig. 2h,k,n) and along  $k_x$  (Fig. 2i,l,o) consistently shows the well-defined energy gap with nearly the same magnitudes within the range of  $\pm 10$  meV, which indicates the isotropy of energy gap (Extended Data Fig. 2 for constant-energy maps).

The key feature of these findings (backward-bending band dispersion and gaplike features) can be naturally explained by the characteristic band structure of liquid metals predicted in theory<sup>1-12</sup>. We employ a single-site (structure-independent) model<sup>12</sup> for multiple scattering (Methods), in which each ion is assumed to be a spherical step potential  $U_s$  whose depth is  $V_0$  and radius is  $r_s$  (Fig. 3a). This may be a crude approximation, but as will be shown below, even this simple model is able to capture the essential feature in the band structure of liquid metals. For the partial wave of  $l \neq 0$ , the sum of ionic  $U_s$  and centrifugal  $U_l$  forms a potential well around each ion. Electron waves scattered by this effective potential

acquire a phase shift  $d_l$  as a function of  $k$ , as shown in Fig. 3b. If  $d_l$  rises through  $\pi/2$  in the  $l^{\text{th}}$  partial wave, the magnitude of scattering amplitude  $f_l$  is peaked at  $k_r$ , which is the characteristic feature of resonance<sup>9</sup> (Fig. 3c). The phase difference between incoming and outgoing waves outside of  $r_s$  is  $2d_l$  that is  $\pi$  at  $k_r$ . Their destructive interference spatially localizes the electron waves in the potential well around each ion, which is the formation of QBS (Fig. 3d).

The variation of complex  $kf_l$  with  $d_l$  is restricted by the unitary relation<sup>29</sup> that can be readily understood by drawing the unitary circle in Fig. 3e. This explains that  $\text{Re}(kf_l)$  and  $\text{Im}(kf_l)$  take the simple form of  $\sin(2d_l)$  and  $\sin^2(d_l)$ , respectively (Fig. 3f). In the theory of liquid metals<sup>1-9</sup> (Methods), a complex  $Dk$  of electron waves acquired by the effect of multiple scattering can be approximately written in terms of the predominant  $f_l$  of the partial wave at resonance as:

$$\Delta k \sim \frac{2\pi n_d f_l}{k} = \frac{2\pi n_d}{k^2} \sin \delta_l e^{i\delta_l}.$$

It follows that  $\text{Re}(Dk)$  and  $\text{Im}(Dk)$  should be directly proportional to  $\sin(2d_l)/k^2$  and  $\sin^2(d_l)/k^2$ , respectively. As depicted in Fig. 3g, the typical quadratic band dispersion of free electrons (dotted line) is distorted by  $\text{Re}(Dk)$  in the sinusoidal form (bold line). The Fourier transform of electrons with complex  $Dk$  is peaked at  $k + \text{Re}(Dk)$ , but spreads over the range of  $\pm \text{Im}(Dk)$  (grey area in Fig. 3g). This spread of  $k$  corresponds to the spatial localization of electrons or QBS in the potential well around each ion (Fig. 3a,d). This is accompanied by changes in the density of states<sup>5,9-12</sup> that is roughly proportional to the energy derivative of  $\text{Re}(Dk)$  (Fig. 3h). The negative slope of band dispersion near  $E_r$  (shown in red) forms a local minimum in the density of states, which is the pseudogap<sup>13,14</sup>. If a residual density of states in the pseudogap is below about 1/3 of that of free electrons<sup>14</sup>, electronic states in the pseudogap are localized as shown in Fig. 3d, so that conductivity vanishes in the sense of Anderson localization<sup>15</sup>.

The resonance scattering, which is characterized by  $d_l$  that rises through  $\pi/2$  (Fig. 3b), occurs in one of the partial waves ( $l=0$ ) for a given  $k_r$  (Extended Data Fig. 3)<sup>9</sup>. Which partial wave is at resonance depends on the depth of scattering potential  $V_0$  (Fig. 3a). As shown in Fig. 4a, there are three distinct  $V_0$  ranges to have the partial wave of  $l=1$  ( $p$ -wave),  $l=2$  ( $d$ -wave), and  $l=3$  ( $f$ -wave) at resonance, respectively. The variation of  $d_l$  with  $k$  is calculated for 3 different  $V_0$ 's to have  $p$ -wave,  $d$ -wave, and  $f$ -wave resonance at the same  $k_r$  (dotted line in Fig. 4a), as compared in Fig. 4b. The rise of  $d_l$  at  $d$ -wave resonance is steeper (narrower in  $k$ ) than that at  $p$ -wave resonance. The corresponding density of states is calculated based on thin-slab approximations (Methods)<sup>12</sup>, which is shown in Fig. 4c. Indeed,  $p$ -wave pseudogap is greater in magnitude than  $d$ -wave pseudogap. Another remarkable difference in Fig. 4b is that  $d_l$  at  $p$ -wave resonance rises through  $\pi/2$  but turns back without reaching close to  $\pi$  (incomplete resonance, Extended Data Fig. 4). This makes  $p$ -wave pseudogap less clear with a residual density of states, as compared to  $d$ -wave pseudogap (Fig. 4c).

The renormalized band structure of liquid metals (Fig. 3g) with its density of states (Fig. 4c) is taken into account to simulate a series of ARPES spectra (Methods) displayed in Fig. 4e-j. The simulated APRES spectra for  $p$ -wave resonance in Fig. 4e-g reproduce the backward-bending dispersion of Na-doped black phosphorus with a diminishing intensity towards  $E_F$  (Fig. 2d-f). This could have been observed owing to the finite density of states in  $p$ -wave pseudogap (red curve in Fig. 4c). On the other hand, the sharp dip of  $d$ -wave pseudogap (yellow curve in Fig. 4c) renders the simulated ARPES spectra in Fig. 4h-j to exhibit a clear gaplike feature with little spectral weight on the backward-bending part of band dispersion, as observed for K, Rb, and Cs in Fig. 2g-o (Extended Data Fig. 5 for a fuller set of simulations). Therefore, our spectral simulations (Fig. 4e-j) not only collectively reproduce key aspects of experimental observations (Fig. 2d-o), but also naturally explain the difference between the Na case and K, Rb, Cs cases by the orbital character of pseudogap,  $p$ -wave or  $d$ -wave.

For the quantitative analysis on the magnitude of pseudogap, the ARPES spectral weight, which is proportional to the density of states, is plotted as a function of energy in Fig. 4d for Na and K (Methods). They commonly show the diminishing spectral weight towards  $E_F$  over different energy scales. The magnitude of pseudogap is defined by the energy at which the spectral weight drops by half relative to  $E_F$ . A fit to data with the calculated density of states (Fig. 4c) multiplied by the Fermi-Dirac distribution function yields the pseudogap of  $235 \pm 53$  meV for Na,  $65 \pm 23$  meV for K,  $65 \pm 17$  meV for Rb, and  $33 \pm 12$  meV for Cs. They are in the range of  $p$ -wave (200-250 meV) and  $d$ -wave (30-80 meV) pseudogaps at their corresponding  $k_r$ , respectively (Fig. 5a). This can be explained by resonance states (or QBS) that are bound to different kinds of alkali metal and should thus follow their respective orbital character. Since Na is a period-3 element with no  $d$  block, the resonance states of Na ions are compelled to have the  $p$ -wave character. On the other hand, K and Rb in periods 4 and 5 have the  $d$  block between  $s$  and  $p$  blocks, and their QBS are naturally expected to have the  $d$ -wave character. The resonance of Cs in period 6 with a  $f$  block prior to the  $d$  block can have either  $d$ -wave or  $f$ -wave character, but the experimental magnitude of pseudogap seems to favour  $d$ -wave resonance (20-50 meV) rather than  $f$ -wave resonance (less than 10 meV).

The magnitude of pseudogap is plotted in Fig. 5b as a function of the dopant density  $n_d$  for different kinds of alkali metal (Extended Data Fig. 6 for a doping series of raw ARPES data). In the wide range of  $n_d$  shown in grey, pseudogap is persistently observed at  $E_F$  with a nearly isotropic magnitude. Since  $k_r$  is inversely proportional to the average interatomic distance of constituent alkali-metal dopants, their spatial distribution should be made to locate a set of  $k_r$  shown by the blue oval in Fig. 1c at the Fermi contour of C1 in Fig. 1d. This implies that the liquid phase of dopants may be energetically favoured to stabilize doped electrons in the adjacent crystalline insulator by the formation of pseudogap in the whole Fermi surface, which is connected to glassy charge-density waves<sup>30</sup>. For an insulator doped by monovalent dopants,  $n_d$  ( $\sim k_r^2$ ) equals to  $n_e$  ( $\sim k_F^2$ ), so that  $k_r$  should follow  $k_F$  with increasing  $n_d$ . However, once the C2 band starts crossing  $E_F$ ,  $n_d$  is no longer equivalent to the  $n_e$  of the C1 band, and the magnitude of pseudogap progressively reduces as observed in Fig. 5b.

It would be difficult to distinguish the ARPES spectra of  $d$ -wave pseudogap (Fig. 4h-j) from those of actual energy gaps caused by any kind of symmetry breaking in crystalline solids. Our systematic observation of both  $p$ -wave and  $d$ -wave pseudogap allows to clearly identify their origin as a characteristic feature in the band structure of liquid metals. This provides a key clue to the pseudogap phase of various materials<sup>16-20</sup>, a common aspect of which is the crystalline insulator doped by disordered (liquid-like) dopants in the charge-reservoir layers. It should be noted again that the backward-bending band dispersion of Na-doped black phosphorus in Fig. 2f even reaches close to  $k = 0$  ( $|Dk|$  is comparable to the magnitude of  $k$ ), as predicted in the self-consistent model proposed by Anderson and McMillan<sup>5</sup>. A potential pairing instability in this band structure might be an interesting topic for future works.

## Methods

**ARPES experiments and analysis.** We conducted ARPES measurements at the Beamline 7.0.2 (MAESTRO), the Advanced Light Source. The microARPES end-station is equipped with a hemispherical spectrometer. We collected the data at the sample temperature of 15-35 K with the photon energy of 104 eV that corresponds to the Z point in the bulk Brillouin zone of black phosphorus<sup>23</sup>. At these settings, energy and  $k$  resolutions are better than 20 meV and  $0.01 \text{ \AA}^{-1}$ , respectively. We carefully aligned the in-plane orientation of black phosphorus along the  $k_y$ ,  $k_s$ , or  $k_x$  direction with respect to the analyser slit within the accuracy of  $\pm 0.5^\circ$ . Then, we repeated the cycle of *in situ* deposition and data acquisition to take a doping series of ARPES data shown in Fig. 2d-o and Extended Data Fig. 6. After converting the emission angle to  $k$ , a series of  $k$  distribution curves at a constant energy was fit with the standard Lorentzian function. The peak area, which is proportional to the spectral weight, is plotted as a function of energy in Fig. 4d. The energy at which the spectral weight drops by half relative to  $E_F$  is taken as the magnitude of pseudogap in Fig 5b.

**Sample preparation and surface doping.** The single-crystal samples of black phosphorus (99.995%, HQ graphene) were glued on sample holders by conductive epoxy. The sample holders were transferred in the ARPES chamber through a semi-automated sample highway system. The black phosphorus samples were cleaved in the ultrahigh vacuum chamber with the base pressure better than  $5 \times 10^{-11}$  torr. We scanned over the surface with the photon beam of 80  $\mu\text{m}$  in diameter to carefully optimize the sharpness of ARPES spectra (Fig. 2d-o). The *in situ* deposition of alkali metals (Na, K, Rb, and Cs) was carried out using commercial dispensers (SAES) at the adsorption rate of over  $3.6 \times 10^{11} \text{ cm}^{-2}/\text{s}$ .  $n_d$  is assumed equivalent to  $n_e$  estimated from the density of surface unit cells ( $6.9 \times 10^{14} \text{ cm}^{-2}$ ) multiplied by the ratio of area enclosed by constant-energy contours at  $E_F$  (Fig. 1d) to that of the surface Brillouin zone. We extrapolate  $k_F$  in  $x$  ( $k_{F,x}$ ) and  $k_F$  in  $y$  ( $k_{F,y}$ ) from the band dispersion of C1, and estimate the area of Fermi contours as  $\pi k_{F,x} k_{F,y}$ . The unit of ML in Fig. 5b is defined as  $4.3 \times 10^{14} \text{ cm}^{-2}$ , which is the density of closely packed K atoms in two dimensions.

**Theoretical model for liquid metals.** We employ the theory of multiple scattering<sup>1-12</sup> by each ion assumed as a spherical step potential whose depth is  $V_0$  and radius is  $r_s$  (Fig. 3a). This boundary-condition problem is solved based on spherical wavefunctions and partial-wave expansion to obtain the phase shift of partial waves  $d_l$  (Fig. 3b). Then, the scattering amplitude of partial waves  $f_l$  can be simply written in terms of  $d_l$  as:

$$f_l = \frac{\sin \delta_l e^{i\delta_l}}{k}.$$

$\text{Re}(kf_l)$  and  $\text{Im}(kf_l)$  take the simple mathematical form of  $\sin(2d_l)$  and  $\sin^2(d_l)$  (Fig. 3f), and their relation can be straightforwardly shown by the unitary circle in the complex plane (Fig. 3e)<sup>29</sup>. The magnitude of  $f_l$  in Fig. 3c is given by  $\sin(d_l)/k$  with its maximum possible value of  $1/k_r$  at resonance. By taking the square of spherical wavefunctions at a constant  $k$ , the probability density is calculated and plotted as a function of  $r$  and  $k$  in Fig. 3d after the normalization of the first peaks outside of  $r_s$ . In the thin-slab approximation ( $k \gg Dk$ , forward scattering)<sup>9,12</sup>,  $Dk$  can be written in terms of the predominant  $f_l$  of the partial wave at resonance as:

$$\Delta k \sim \frac{2\pi n_d f_l}{k}.$$

It follows that  $\text{Re}(Dk)$  and  $\text{Im}(Dk)$  are directly proportional to  $\sin(2d_l)/k^2$  and  $\sin^2(d_l)/k^2$  with respect to  $k_r$ , respectively. The quadratic band structure of  $E \sim k^2$  is renormalized by  $\text{Re}(Dk)$  as  $k' = k + \text{Re}(Dk)$  with the spread of  $k'$  over the range of  $\pm \text{Im}(Dk)$ , which is the band structure of liquid metals depicted in Fig. 3g.

The resonance scattering, which is characterized by  $d_l$  that passes through  $\pi/2$ , occurs in one of the partial waves for a given  $k_r$ . Which partial wave is at resonance scattering depends on the depth of scattering potential  $V_0$  in Fig. 3a. For a constant  $V_0$  (set to 16.4 eV for  $d$ -wave resonance), a partial-wave series of  $d_l$  and  $Dk$  is calculated as described above and displayed in Extended Data Fig. 3. We systematically calculated  $p$ -wave,  $d$ -wave, and  $f$ -wave resonance as a function of  $V_0$  with the constant  $r_s$  (set to 2.1 Å for liquid Na<sup>31</sup>), as shown in Fig. 4a. The representative set of  $d_l$  at  $p$ -wave,  $d$ -wave, and  $f$ -wave resonance in Fig. 4b is calculated for  $V_0 = 7.4$  eV, 16.4 eV, and 27.8 eV to have the same  $k_r$  of 0.36 Å<sup>-1</sup> (Extended Data Fig. 4 for the fuller set of  $U_l$ ,  $d_l$ , and  $Dk$ ). From those of  $p$ -wave and  $d$ -wave resonance, the density of states in Fig. 4c is calculated as described in Ref. <sup>12</sup>. The half width at half maximum of  $\text{Im}(Dk)$ , which corresponds to half the dip width in the energy derivative of  $\text{Re}(Dk)$  in Fig. 3h, is taken as the magnitude of pseudogap in Fig. 5a.

**Spectral simulations.** The experimental band structure of liquid metals is simulated based on the model of  $k$  renormalizations described above. Each  $k$  distribution of ARPES intensity  $I_E$  can be approximately modelled in the form of the standard Lorentzian function as:

$$I_E(k') \sim \frac{[\text{Im}(\Delta k)_E + \eta]}{[k' - k_E - \text{Re}(\Delta k)_E]^2 + [\text{Im}(\Delta k)_E + \eta]^2} \cdot f_{\text{FD}} \cdot n_E$$

where  $k_E$  is the dispersion of non-interacting bands in a form of  $E \sim k^p$  with  $k_F$  and the bottom energy taken from ARPES data.  $p$  is set to 1.8-2.0 (quadratic) in  $y$  and 1.2-1.4 (nearly linear) in  $x$  to reflect the well-known armchair-zigzag anisotropy of black phosphorus<sup>23</sup>.  $\text{Re}(Dk)$  and  $\text{Im}(Dk)$  are taken in a form of  $\sin(2d)/k^2$  and  $\sin^2(d)/k^2$ , respectively, with respect to  $k_r$  located at  $k_F$ . The magnitude of  $\text{Re}(Dk)$  and  $\text{Im}(Dk)$  is scaled to fit the spectral peak position and width of ARPES spectra.  $h$  is the offset  $k$  broadening in the range of 0.03-0.14  $\text{\AA}^{-1}$ , and  $f_{\text{FD}}$  is the Fermi-Dirac distribution function.  $n_E$  is the factor that accounts for the diminishing density of states towards  $E_F$  (pseudogap), calculated for  $p$ -wave and  $d$ -wave resonance and scaled to the experimental spectral weight (black lines in Fig. 4d). The simulated spectra in this way are shown in Fig. 4e-j, and directly compared to a fuller set of data in Extended Data Fig. 5.

**Structural simulations.** The liquid phase of atoms with only short-range order is simulated based on the hard-sphere model. Each atom is constructed by a two-dimensional Gaussian function with the width of 1.5  $\text{\AA}$ . The 7200 atoms are randomly distributed over the area of 150  $\times$  150  $\text{nm}^2$  under the condition that the interatomic spacing cannot be smaller than  $d$ .  $d$  is set to 1.9 nm in the  $x$  direction and to 0.42  $\times$  1.9 nm in the  $y$  direction to take into account the anisotropy of  $k_{F,x}/k_{F,y}$  (Fig. 1d), as discussed in Ref. <sup>25,26</sup>. The fast Fourier transform is used to simulate the reciprocal-space lattice structure in Fig. 1c, which is in good agreement with the previous report<sup>25</sup>. The simulated lattice structure of liquid phases with short-range order is compared to the perfect crystal with long-range order and the fully random phase with no short-range order in Extended Data Fig. 1.

## Data availability

The data that support the findings of this study are available from the corresponding author on reasonable request.

## Declarations

## Author contributions

S.H.R., M.H., and D.Y.P. performed ARPES experiments with help from C.J., E.R., and A.B. S.H.R. and M.H. performed model calculations and simulations with help from D.Y.P. K.S.K. conceived and directed the project. S.H.R., M.H., D.Y.P., and K.S.K. wrote the manuscript with contributions from all other co-authors.

## Acknowledgements

We thank S. -S. Baik, Y. -W. Son, and E. -G. Moon for helpful discussions. This work was supported by the National Research Foundation (NRF) of Korea (Grants No. NRF-2020R1A2C2102469, NRF-2017R1A5A1014862, NRF-2020K1A3A7A09080364), and the Future-leading Research Initiative of Yonsei University (2019-22-0079). The Advanced Light Source was supported by the U. S. Department of Energy, Office of Sciences under Contract No. DE-AC02-05CH11231.

## Data availability

The data that support the findings of this study are available from the corresponding author on reasonable request.

## Competing interests

The authors declare no competing interests.

## Correspondence and requests for materials

should be addressed to K.S.K.

## Reprints and permissions information

is available at [www.nature.com/reprints](http://www.nature.com/reprints).

## References

1. Edwards, S. F. The electronic structure of disordered systems. *Phil. Mag.* **6**, 617 (1961). <https://doi.org/10.1080/14786436108244414>
2. Edwards, S. F. The electronic structure of liquid metals. *Proc. Roy. Soc. A* **267**, 518 (1962). <https://doi.org/10.1098/rspa.1962.0116>
3. Ziman, J. M. A theory of the electrical properties of liquid metals. I: The monovalent metals. *Phil. Mag.* **6**, 1013 (1961). <https://doi.org/10.1080/14786436108243361>
4. Ziman, J. M. The  $T$  matrix, the  $K$  matrix, d bands and  $l$ -dependent pseudo-potentials in the theory of metals. *Proc. Phys. Soc.* **86**, 337 (1965). <https://doi.org/10.1088/0370-1328/86/2/311>
5. Anderson, P. W. & McMillan, W. L. *Multiple-Scattering Theory and Resonances in Transition Metals, Proceedings of the International School of Physics "Enrico Fermi" Course 37*, edited by Marshall, W. (Academic, New York, 1967). [https://doi.org/10.1142/9789812385123\\_0013](https://doi.org/10.1142/9789812385123_0013)
6. Morgan, G. J. Electron transport in liquid metals II. A model for the wave functions in liquid transition metals. *J. Phys. C: Solid State Phys.* **2**, 1454 (1969). <https://doi.org/10.1088/0022-3719/2/8/314>

7. Gyorffy, B. L. Electronic states in liquid metals: A generalization of the coherent-potential approximation for a system with short-range order. *Phys. Rev. B* **1**, 3290 (1970).  
<https://doi.org/10.1103/PhysRevB.1.3290>
8. Schwartz, L. & Ehrenreich, H. Single-site approximations in the electronic theory of liquid metals. *Ann. Phys.* **64**, 100 (1971). [https://doi.org/10.1016/0003-4916\(71\)90281-8](https://doi.org/10.1016/0003-4916(71)90281-8)
9. Faber, T. E. *An introduction to the theory of liquid metals*. (Cambridge University Press, 1972).
10. Olson, J. J. Anderson-McMillan prescription for the density of states of liquid iron. *Phys. Rev. B* **12**, 2908 (1975). <https://doi.org/10.1103/PhysRevB.12.2908>
11. Chang, K. S., Sher, A., Petzinger, K. G. & Weisz, G. Density of states of liquid Cu. *Phys. Rev. B* **12**, 5506 (1975). <https://doi.org/10.1103/PhysRevB.12.5506>
12. Oglesby, J. & Lloyd, P. Some single-site structure-independent approximations in condensed materials. *J. Phys. C: Solid State Phys.* **9**, 2879 (1976). <http://doi.org/10.1088/0022-3719/9/15/010>
13. Mott, N. F. Metal-insulator transition. *Rev. Mod. Phys.* **40**, 677 (1968). <https://doi.org/10.1103/RevModPhys.40.677>
14. Mott, N. F. Conduction in non-crystalline materials: III. Localized states in a pseudogap and near extremities of conduction and valence bands. *Phil. Mag.* **19**, 835 (1968).  
<https://doi.org/10.1080/14786436908216338>
15. Anderson, P. W. Absence of diffusion in certain random lattices. *Phys. Rev.* **109**, 1492 (1958).  
<https://doi.org/10.1103/PhysRev.109.1492>
16. Damascelli, A., Hussain, Z. & Shen, Z. -X. Angle-resolved photoemission studies of the cuprate superconductors. *Rev. Mod. Phys.* **75**, 473 (2003). <https://doi.org/10.1103/RevModPhys.75.473>
17. Mannella, N. *et al.* Nodal quasiparticle in pseudogapped colossal magnetoresistive manganites. *Nature* **438**, 474 (2005). <https://doi.org/10.1038/nature04273>
18. Sacépé, B., Chapelier, C., Baturina, T. I., Vinokur, V. M., Baklanov, M. R. & Sanquer, M. Pseudogap in a thin film of a conventional superconductor. *Nat. Commun.* **1**, 140 (2010).  
<https://doi.org/10.1038/ncomms1140>
19. Uchida, M. *et al.* Pseudogap of metallic layered nickelate  $R_{2-x}Sr_xNiO_4$  ( $R = Nd, Eu$ ) crystals measured using angle-resolved photoemission spectroscopy. *Phys. Rev. Lett.* **106**, 027001 (2011).  
<https://doi.org/10.1103/PhysRevLett.106.027001>
20. Kim, Y. K., Sung, N. H., Denlinger, J. D. & Kim, B. J. Observation of a  $d$ -wave gap in electron-doped  $Sr_2IrO_4$ . *Nat. Phys.* **12**, 37 (2016). <https://doi.org/10.1038/NPHYS3503>
21. Baumberger, F., Auwärter, W., Greber, T. & Osterwalder, J. Electron coherence in a melting lead monolayer. *Science* **306**, 2221 (2004). <https://doi.org/10.1126/science.1103984>
22. Kim, K. S. & Yeom, H. W. Radial band structure of electrons in liquid metals. *Phys. Rev. Lett.* **107**, 136402 (2011). <https://doi.org/10.1103/PhysRevLett.107.136402>
23. Kim, J. *et al.* Observation of tunable band gap and anisotropic Dirac semimetal state in black phosphorus. *Science* **349**, 723 (2015). <https://doi.org/10.1126/science.aaa6486>

24. Baik, S. S., Kim, K. S., Yi, Y. & Choi, H. J. Emergence of two-dimensional massless Dirac fermions, chiral pseudospins, and Berry's phase in potassium doped few-layer black phosphorus. *Nano Lett.* **15**, 7788 (2015). <https://doi.org/10.1021/acs.nanolett.5b04106>
25. Kiraly, B. *et al.* Anisotropic two-dimensional screening at the surface of black phosphorus. *Phys. Rev. Lett.* **123**, 216403 (2019). <https://doi.org/10.1103/PhysRevLett.123.216403>
26. Tian, Z. *et al.* Isotropic charge screening of anisotropic black phosphorus revealed by potassium adatoms. *Phys. Rev. B* **100**, 085440 (2019). <https://doi.org/10.1103/PhysRevB.100.085440>
27. Negulyaev, N. N. *et al.* Melting of two-dimensional adatom superlattices stabilized by long-range electronic interactions. *Phys. Rev. Lett.* **102**, 246102 (2009). <https://doi.org/10.1103/PhysRevLett.102.246102>
28. Hirata, A. *et al.* Direct observation of local atomic order in a metallic glass. *Nat. Mater.* **10**, 28 (2011). <https://doi.org/10.1038/nmat2897>
29. Sakurai, J. J. & Napolitano, J. *Modern Quantum Mechanics* (Cambridge University Press, 2017). <https://doi.org/10.1017/9781108499996>
30. Kang, M. *et al.* Evolution of charge order topology across a magnetic phase transition in cuprate superconductors. *Nat. Phys.* **15**, 335 (2019). <https://doi.org/10.1038/s41567-018-0401-8>
31. March, N. H. *Liquid Metals*. (Cambridge University Press, 1990).

## Figures

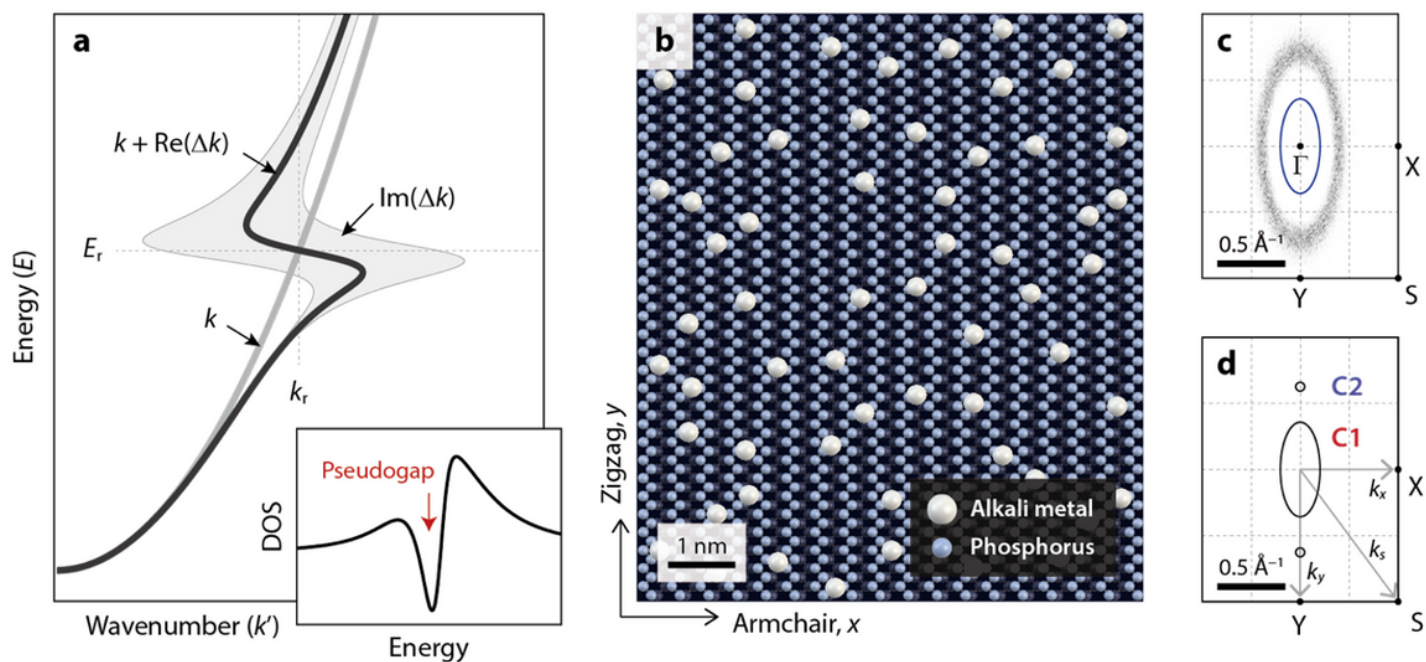


**Figure 1**

Band structure of liquid metals on a crystalline insulator. a, Electronic band structure predicted in the theory of liquid metals<sup>1-12</sup>. The black bold line shows a dispersion relation of energy ( $E$ ) versus  $k$

renormalized by  $\text{Re}(\Delta k)$  from the quadratic band structure of free electrons ( $E \sim k^2$ ) shown by the grey bold line. The grey region represents the spread of  $k$  over the range of  $\pm \text{Im}(\Delta k)$  with respect to  $E_r$  and  $k_r$ . Inset shows the corresponding density of states as a result of  $k$  renormalizations. b, Schematics of liquid dopants (alkali metals) on a crystalline insulator (black phosphorus) with its crystallographic direction indicated at the bottom left. c, Fourier-transform image taken from the distribution of liquid dopants in b (Methods) to show their reciprocal lattice. The blue oval is a set of half the reciprocal lattice vectors in every in-plane  $k$  direction, which corresponds to  $k_r$  in the model of liquid metals. d, Constant-energy contours at  $E_F$  expected for black phosphorus whose surface is doped at  $n_e = 1.0 \times 10^{14} \text{ cm}^{-2}$  and plotted over the surface Brillouin zone. The grey arrows indicate 3 high-symmetry  $k$  cuts along which a series of ARPES data shown in Fig. 2 is taken.

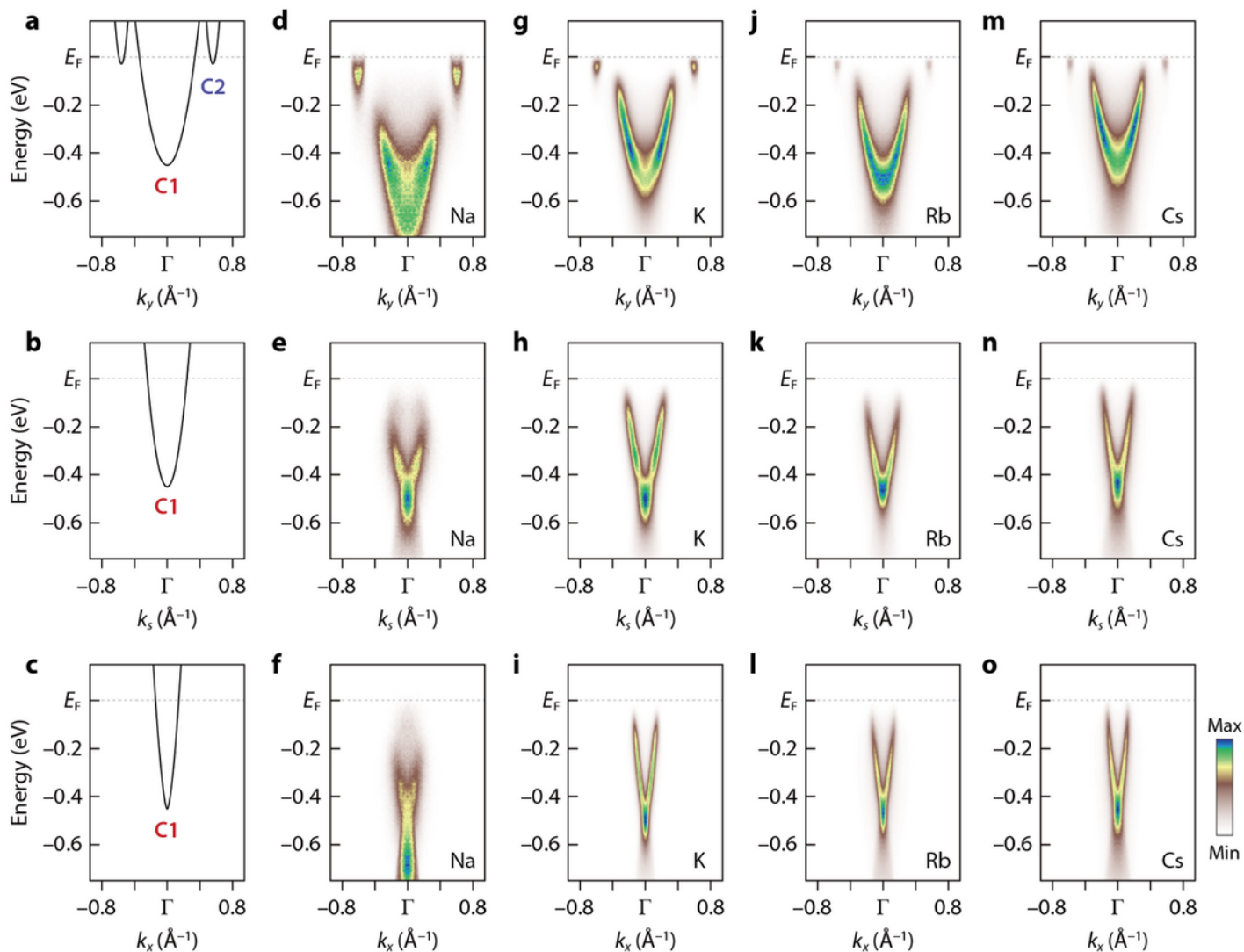


**Figure 2**

Electronic band structure of black phosphorus doped by liquid alkali metals. a-c, Conduction bands of black phosphorus doped to locate  $E_F$  at the bottom of C2 bands ( $n_e = 1.0 \times 10^{14} \text{ cm}^{-2}$ ), shown along  $k_y$  (a),  $k_s$  (b), and  $k_x$  (c) indicated by grey arrows in Fig. 1d. d-o, Corresponding experimental band structure of bulk black phosphorus whose surface is doped by different kinds of alkali metal, Na (d-f), K (g-i), Rb (j-

l), and Cs (m-o), as marked at the bottom right of each panel. This series of data is measured by ARPES at 15–35 K with the photon energy of 104 eV along  $k_y$  (top row),  $k_s$  (middle row), and  $k_x$  (bottom row).

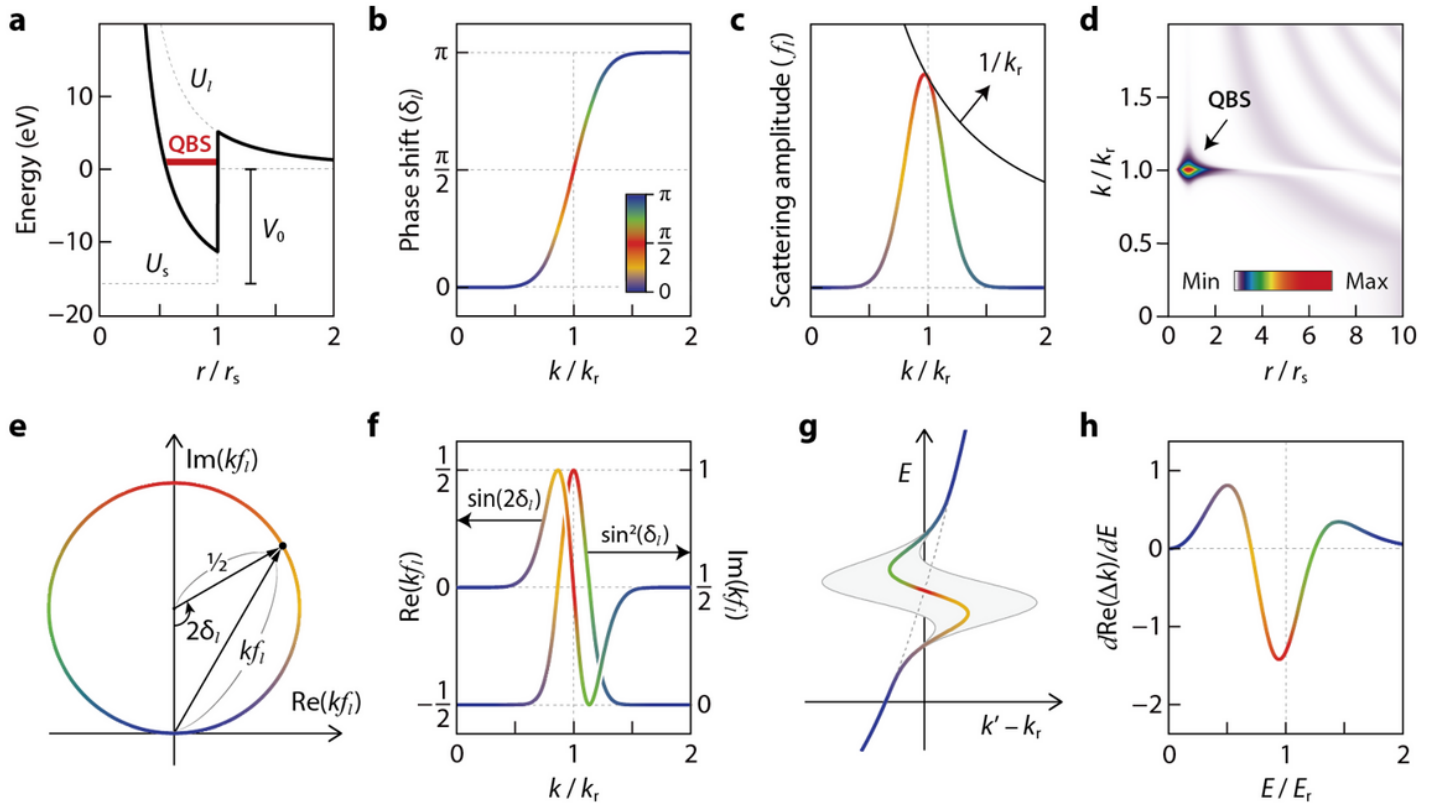


**Figure 3**

Resonance scattering in liquid metals and band renormalizations. a, Effective scattering potential (bold line) composed of the ionic potential (dotted line marked by  $U_s$ ) and the centrifugal potential (dotted line marked by  $U_i$ ).  $U_s$  is assumed as a step potential whose depth is  $V_0$  and width is  $r_s$ . b, Phase shift  $\delta_i$  simulated in the form of sigmoid that rises from 0 to  $\pi$  through  $\pi/2$  at  $k r$ . c, Magnitude of the scattering amplitude  $f_l$  calculated from  $\delta_i$  in b by  $\sin(\delta_i)/k$ . The black line is a trace of  $f_l$  at resonance with  $k r$ . d, k series of a probability density calculated for spherical waves in the effective potential in a (Methods). e, Argand diagram of  $k_f l$  with the argument of  $2\delta_i$ . f,  $\text{Re}(k_f l)$  and  $\text{Im}(k_f l)$  calculated from  $\delta_i$  in b in the form of  $\sin(2\delta_i)$  and  $\sin^2(\delta_i)$ , respectively. The relation of  $\text{Re}(k_f l)$  and  $\text{Im}(k_f l)$  can be understood by the unitary circle with a radius of  $1/2$  in e. g, Band renormalizations in liquid metals: The quadratic band structure of free electrons (dotted line) is renormalized by  $\text{Re}(\Delta k)$  (bold line) with a spread of  $k$  over the range of  $\pm \text{Im}(\Delta k)$  (grey area). h, Energy derivative of  $\text{Re}(\Delta k)$  shown with respect to  $E_r$ .  $\delta_i$  is colour-coded as indicated at the bottom right of b, which is used to represent the corresponding value of  $\delta_i$  in c and e-h.

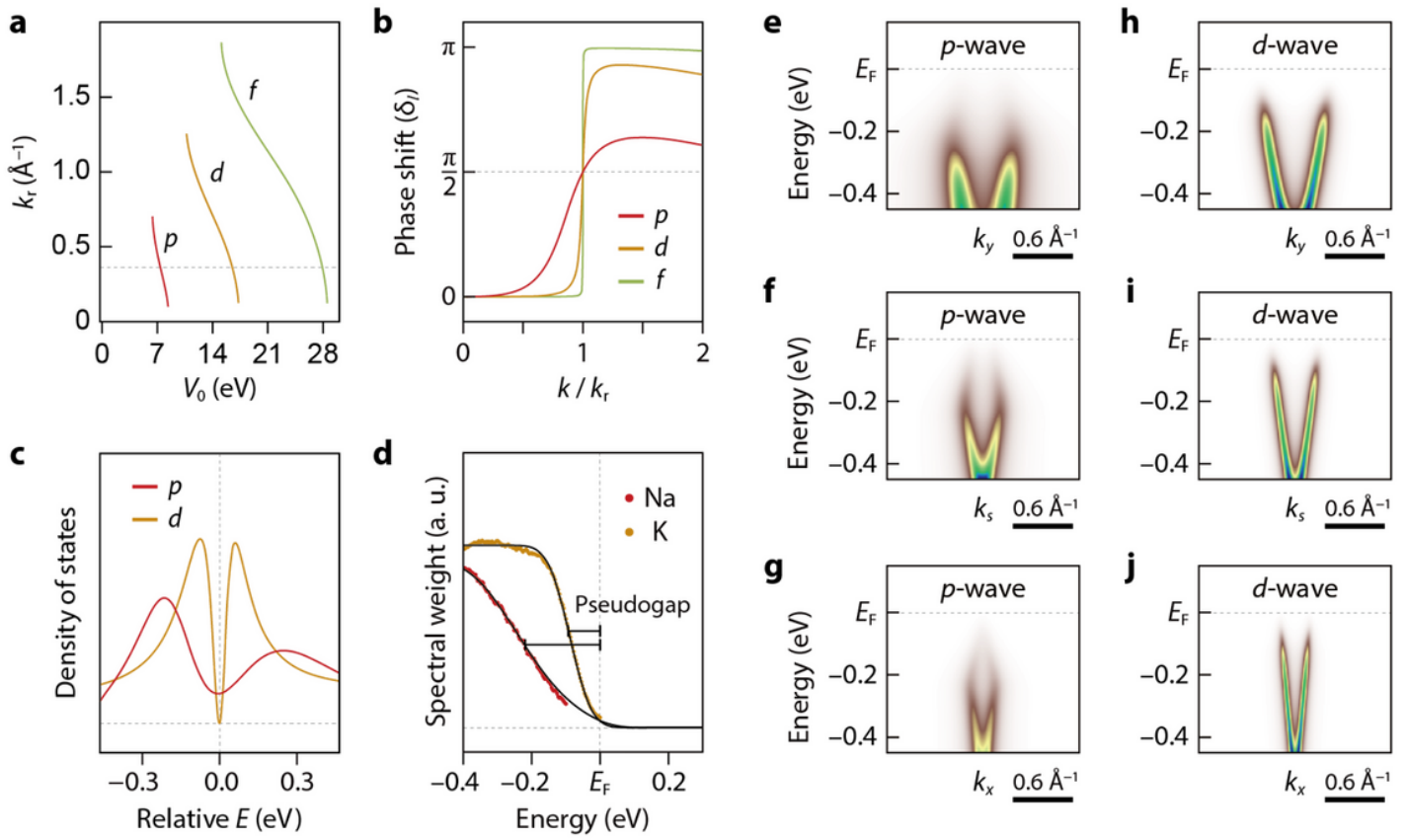


**Figure 4**

Density of states in liquid metals and spectral simulations. a, Potential depth ( $V_0$  in Fig. 3a) to have p-wave, d-wave, and f-wave resonance in the model of liquid metals (Methods). b, Comparison of  $\delta l$  for p-wave ( $l = 1$ ), d-wave ( $l = 2$ ), and f-wave ( $l = 3$ ) resonance calculated for 3 different  $V_0$ 's to have the same  $k_r$  indicated by the dotted line in a. c, Density of states calculated for p-wave and d-wave resonance (Methods) and plotted in  $E$  relative to the local minimum (pseudogap). d, Experimental spectral weight obtained by the curve fit analysis of ARPES data in Fig. 2d,i. The black lines overlaid are a fit to the experimental data with the calculated density of states in c, multiplied by the Fermi-Dirac distribution function. The scale bars are the magnitude of pseudogap defined by the energy at which the spectral weight drops by half relative to  $E_F$ . e-j, Spectral simulation of p-wave (e-g) and d-wave (h-j) resonance (Methods) shown along  $k_y$  (top row),  $k_s$  (middle row), and  $k_x$  (bottom row).

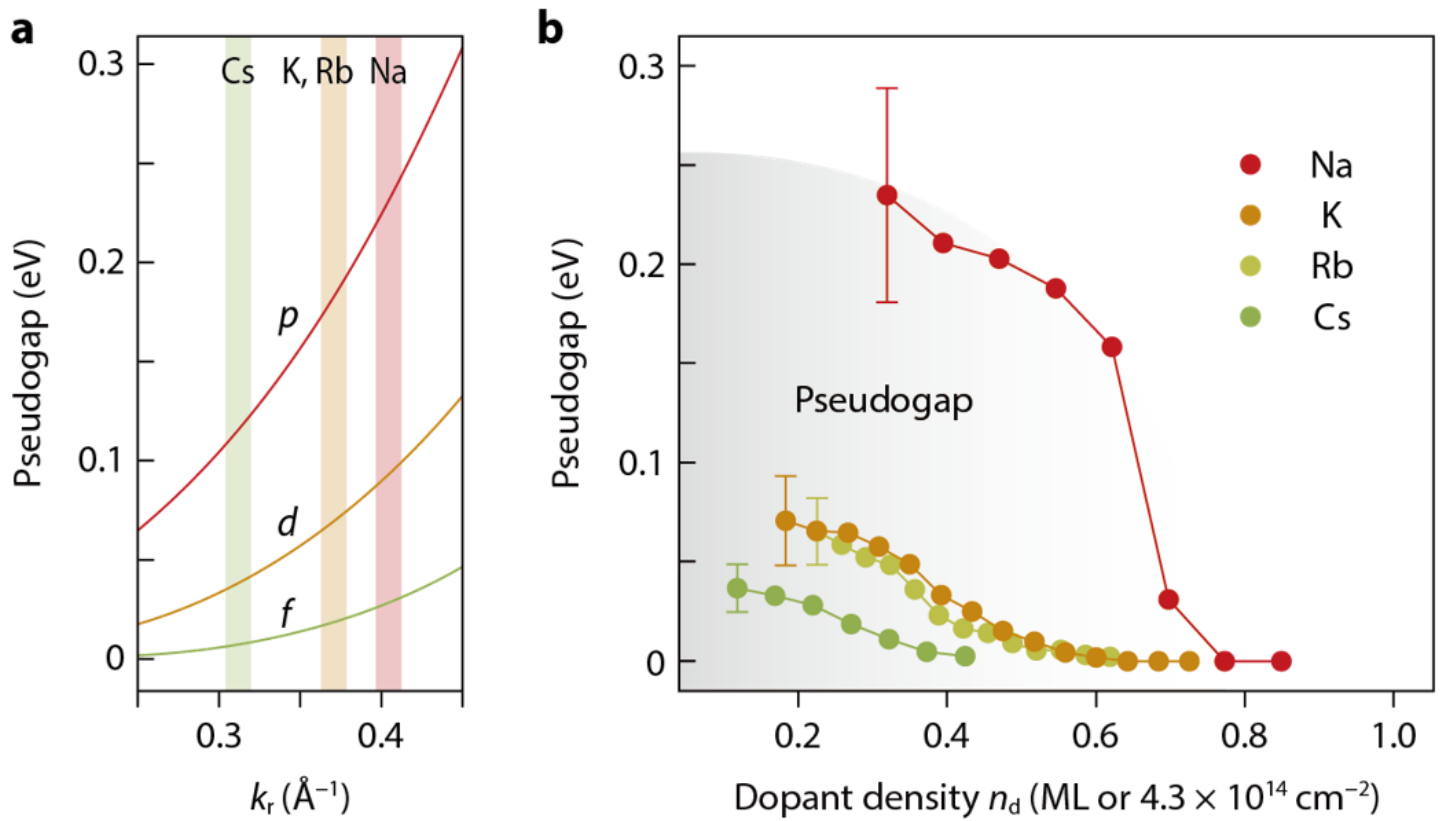


**Figure 5**

Pseudogap of liquid metals and phase diagram. a, Magnitude of pseudogap calculated for p-wave, d-wave, and f-wave resonance with  $k_r$  in Fig. 4a. The vertical stripes marked by Na, K, Rb, and Cs are their respective range of  $k_r$ , in which a maximal pseudogap is observed in experiments. b, Magnitude of pseudogap estimated from ARPES data of black phosphorus doped by Na, K, Rb, and Cs (Extended Data Fig. 6), which is plotted as a function of  $n_d$  over the range of 0–1 ML. The grey area represents the pseudogap phase.

## Supplementary Files

This is a list of supplementary files associated with this preprint. Click to download.

- [Sl.docx](#)